FULL PAPER

Comparison of shadow models and their impact on precise orbit determination of BeiDou satellites during eclipsing phases

Yan Zhang[1,2,4], Xiaoya Wang[1,2,3*] , Kewei Xi[1,2] and Zhen Li[5]

Abstract

Solar radiation pressure (SRP) is an extremely critical perturbative force that affects the GNSS satellites' precise orbit determination (POD). Its imperfect modelling is one of the main error sources of POD, whose magnitude is even to 10^{-9} m/s^2. The shadow factor (i.e., eclipse factor) is one crucial parameter of SRP, generally estimated by the cylindrical model, the conical model, or shadow models considering the Earth's oblateness and the atmospheric effect, such as the Perspective Projection Method atmosphere (PPMatm) model and Solar radiation pressure with Oblateness and Lower Atmospheric Absorption, Refraction, and Scattering Curve Fit (SOLAARS-CF) model. This paper applies the former four shadow models to determine the corresponding precise orbit using BeiDou satellites' ground-based observation, and then compared and assessed the orbit accuracy through Satellite Laser Ranging (SLR) validation and Inter-Satellite Link (ISL) check. The results show that the PPMatm model's accuracy is equivalent to the SOLAARS-CF model. Compared with the conical shadow model, SLR validations show the orbit accuracy from the PPMatm and SOLAARS-CF model can be generally improved by 2–10 mm; ISL range check shows that the Root Mean Square (RMS) can be decreased by 2–7 mm. These results show that the shadow model in GNSS POD should fully consider the Earth's oblateness and the atmospheric effect, especially for the perturbative acceleration higher than 10^{-10} m/s^2.

Keywords: Shadow model, Earth's oblateness, Atmospheric effect, SLR, Inter-satellite link

*Correspondence: wxy@shao.ac.cn
[1] Astro-Geodynamics Research Center, Shanghai Astronomical Observatory,
Chinese Academy of Sciences, Shanghai 200030, China
Full list of author information is available at the end of the article

Zhang *et al. Earth, Planets and Space*   (2022) 74:126

Page 2 of 14

Graphical Abstract

The performance of
different shadow models
with shadow factor and
solar radiation pressure
acceleration (Regard C01
as an example)
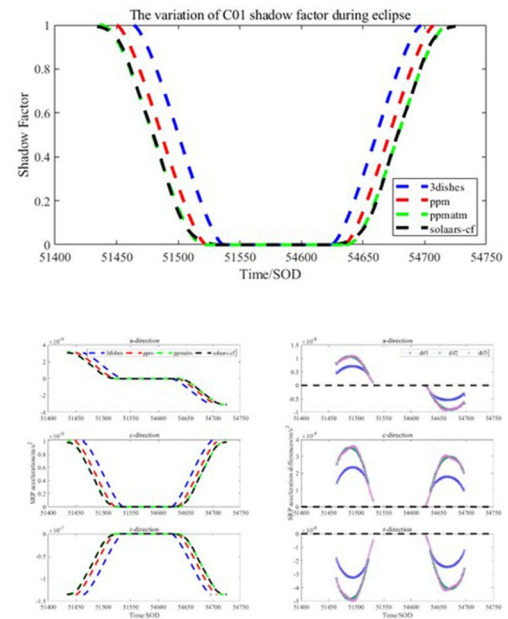
Introduction

Solar radiation pressure is a primary error source in orbit determination of navigation satellites, and it varies with the irradiated area, mass, satellite attitude, the surface optical property of satellites, solar irradiance, etc. (Musen 1960; Rodriguez-Solano et al. 2012; Zhang et al. 2019; Villiger and Dach 2021). The shadow factor (i.e., eclipse factor) is one important parameter related to the irradiated area and is an essential factor of SRP. An eclipse occurs when the Earth or the Moon blocks the sunlight to the satellites. A satellite can confront three phases depending on its relative positions to the Earth/Moon and the Sun. If the satellite is fully exposed to sunlight without any block area, it is in the full phase with the shadow factor 1. When the satellite moves partly behind the Earth, it enters the penumbra phase with the shadow factor between 0 and 1. Alternatively, the shadow factor is set zero when the satellite is completely occluded by the Earth or Moon and cannot receive any sunlight which is termed the umbra phase.

The shadow factor is calculated based on the type of the Earth's shadow towards the Sun. Kozai (1963)

first discovered and discussed the shadow function by proposing a discontinuous step function to depict the penumbra transition and evaluate the influence on the satellite orbit determination. Ferraz-Mello (1972) put forward the cylinder shadow model, a discontinuous shadow function with only two phases: full and umbra phases. The cylinder model ignored the penumbra, resulting in a significant deviation of orbit determination. Hubaux et al. (2012) proposed a cone shadow model that defined penumbra regions and used a hyperbolic tangent sigmoidal function with scaled parameters to ensure the width of the 0–1 S-shaped curve equals to the time that satellites spent across the penumbra. Adhya et al. (2004) proposed a relatively simple method to add the Earth's oblateness modelling. They estimated the phases by the number of line intersection points between the satellite to the Sun-edge points and the Earth. When there was no intersection point, the satellite was in the full phase; when there was an intersection point, the satellite was in the penumbra; when there were two intersection points, the satellite was in the umbra. Vokrouhlicky et al. (1993) redefined the position and radius of the Earth by the

positional relationship between Sunlight, Earth, and satellite, thereby determined the osculating spherical surface of the Earth, which matches the radius of curvature of the circular Earth at the grazing point. Robertson and Shoemaker (2014) corrected the derivation of the formula of Vokrouhlicky et al. (1996) and compensated the Earth's oblateness based on Adhya et al. (2004) and Vokrouhlicky et al. (1994). Robertson and Shoemaker (2014) presented a shadow model (SOLAARS-CF) accounting for Earth's oblateness and atmospheric effect by curve fitting based on a physics-based model (SOLAARS). The SOLAARS model fully integrated the atmospheric extinction modelling (including Rayleigh scattering, aerosol extinction, molecular absorption, and cloud extinction) and the Earth's oblateness, but it was complex and computational. The SOLAARS-CF model significantly reduced the data and computation cost. Inspired by the perspective projection algorithm proposed by Oswald et al. (1982), Li et al. (2019) built PPM and PPMatm shadow models. The difference of PPM and PPMatm is that the latter adds modelling of atmospheric effects.

As discussed above, the cylinder and conical shadow models supposed the Earth is spheric and meanwhile neglected the atmospheric effects. Due to the omission of the penumbra, the cylinder shadow model is seldom applied and the cone shadow model has got widely used relatively in POD. However, Global Geodetic Observing System (GGOS) requires the future Terrestrial Reference Frame (TRF) with a space benchmark of 1 mm and stability of 0.1 mm/year. It means the orbit accuracy needs to be improved to the millimetre level. Therefore, this paper would like to consider the Earth's oblateness and atmospheric effect to refine the solar radiation pressure model using four shadow models (conical, PPM, PPMatm, and SOLAARS-CF) and further study their impact on the SRP and the POD of BeiDou satellites. Finally, their impact and performance are validated not only by SLR orbit validation but also by a new method of ISL for orbit check.

Methodology

The details of four shadow models are described in "Shadow models" section, including the conical shadow model, PPM, PPMatm, and SOLAARS-CF model. The conical shadow model does not contain oblateness and atmospheric effect. PPM lacks atmospheric effect compared with the latter two models. The four shadow models are, respectively, applied in the POD of BDS. Their POD results are compared and validated by SLR orbit validation and the ISL check. The validation method is introduced in section "Validation method".

Shadow models
Conical shadow model

Compared to the cylindrical shadow model, the conical shadow model has a more precise physical meaning and considers the penumbra phase. Apart from occultations of the Sun by the Earth, the Moon's shadow is also considered. The conical model is generic and may well adapted to compute the eclipse conditions, generally applied to the Earth or the Moon as occulting bodies. In this paper, this conical model is named "3dishes". When the occultation has no common part between the Earth and the Moon, the shadow factor can be dealt with the Sun occulted by a spherical body (Montenbruck and Gill 2002). Figure 1 shows the occultation of the Sun by the Earth and the Moon. The occulted area A_0 and the remaining fraction of sunlight $\widetilde{\gamma}_0$ can be expressed as

$$A_0 = A_{FF'} + A_{HH'} - A_{F'G'H'} \quad \widetilde{\gamma}_0 = 1 - \frac{A_0}{\pi \alpha_s^2}, \quad (2.1)$$

PPM and PPMatm shadow model

PPM and PPMatm shadow models are built on the basis of the perspective projection method, which establishes the relationship between the satellite, the Earth, and the Sun in eclipse by a 3D projection. The method makes objects appear effectively to the human eye; thus,
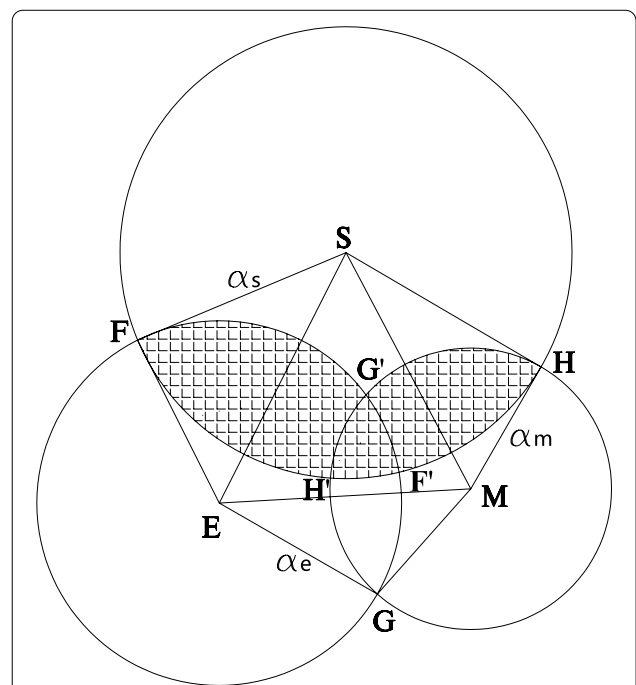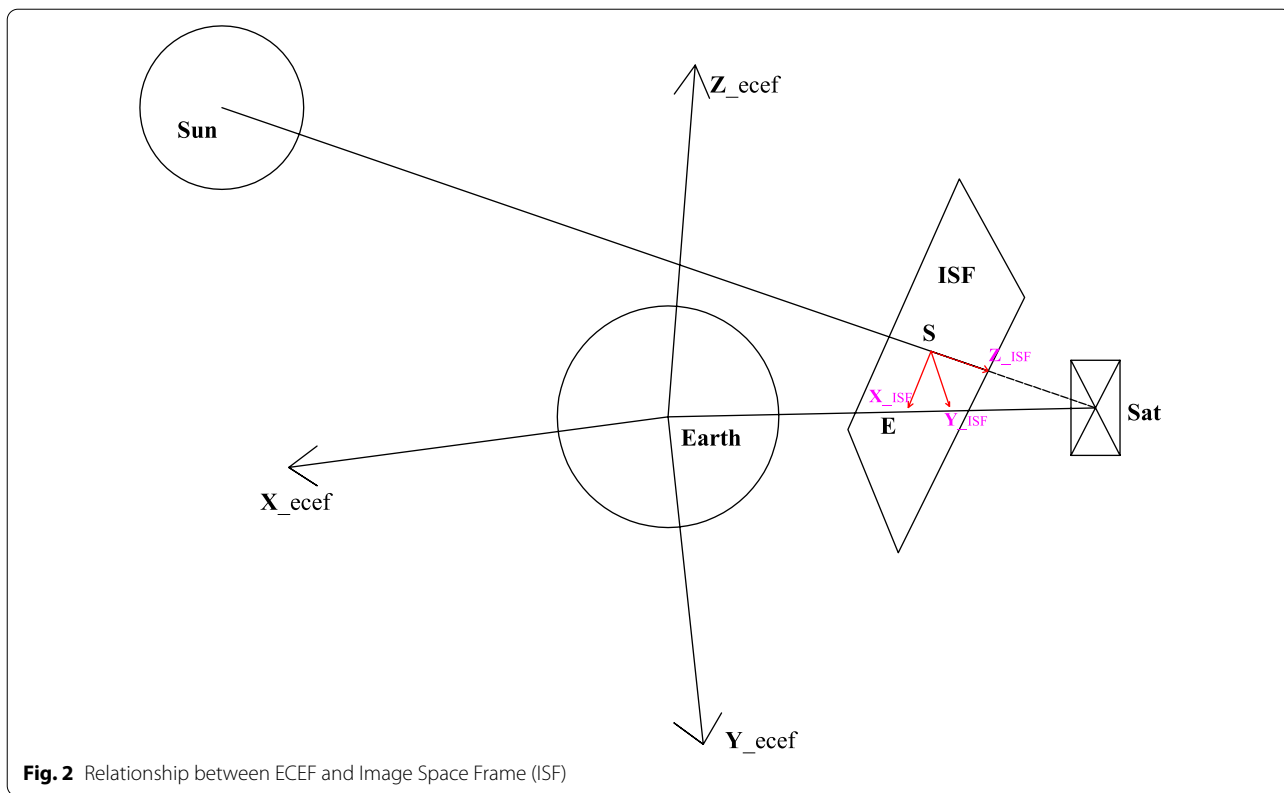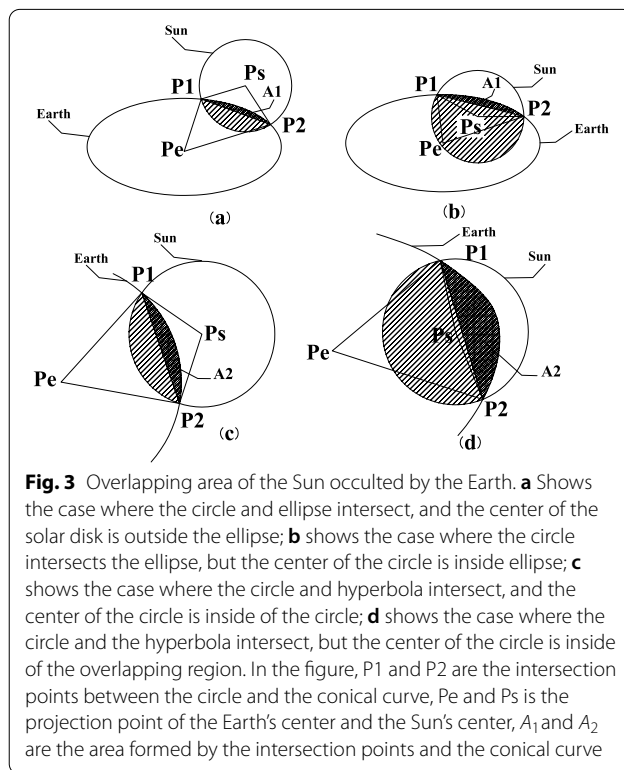

Fig. 1 Occultation of the Sun by the Earth and the Moon (S: the Sun; E: the Earth; M: the Moon). α_s, α_e and α_m stand for the radius of the Sun, the Earth, and the Moon

Fig. 2 Relationship between ECEF and Image Space Frame (ISF)

perspective projection can calculate the overlapping area between the Sun's and Earth's images.

A new frame system named Image Space Frame (ISF) was established to describe the perspective projection method, as shown in Fig. 2. The origin of ISF is located at the position, where the centre of the Sun is projected on the projection plane, the *Z*-axis points from the Sun to the satellite, the *X*-axis points from the origin of ISF to the projection point of the Earth's mass centre, the *Y*-axis lies in the image plane and completes the right-hand coordinate system. X_ecef, Y_ecef, and Z_ecef stand for the axis of the Earth Centred Earth Fixed (ECEF) coordinate system, respectively. The Sun's projection on the image plane is a circle. In the penumbra, the shadow area of the apparent solar disk can be described by the overlapping area, which could be calculated by the sector area A_1 and A_2, shown in Fig. 3. The shape of the conical curve includes an ellipse and hyperbola determined by the condition if the Sun's center is inside the Earth's image or not (Li et al. 2019). The intersection of Earth's projection and Sun's projection can be computed by combining their projection equations, and the shadow factor is calculated by the ratio of the remaining bright area to the total bright area. Then, the PPM shadow model with perspective projection is completed.

Fig. 3 Overlapping area of the Sun occulted by the Earth. **a** Shows the case where the circle and ellipse intersect, and the center of the solar disk is outside the ellipse; **b** shows the case where the circle intersects the ellipse, but the center of the circle is inside ellipse; **c** shows the case where the circle and hyperbola intersect, and the center of the circle is inside of the circle; **d** shows the case where the circle and the hyperbola intersect, but the center of the circle is inside of the overlapping region. In the figure, P1 and P2 are the intersection points between the circle and the conical curve, Pe and Ps is the projection point of the Earth's center and the Sun's center, A_1 and A_2 are the area formed by the intersection points and the conical curve

The PPMatm shadow model considers the change of solar radiation in the atmosphere based on the PPM model. It regarded radiation reduction as a linear function defined as

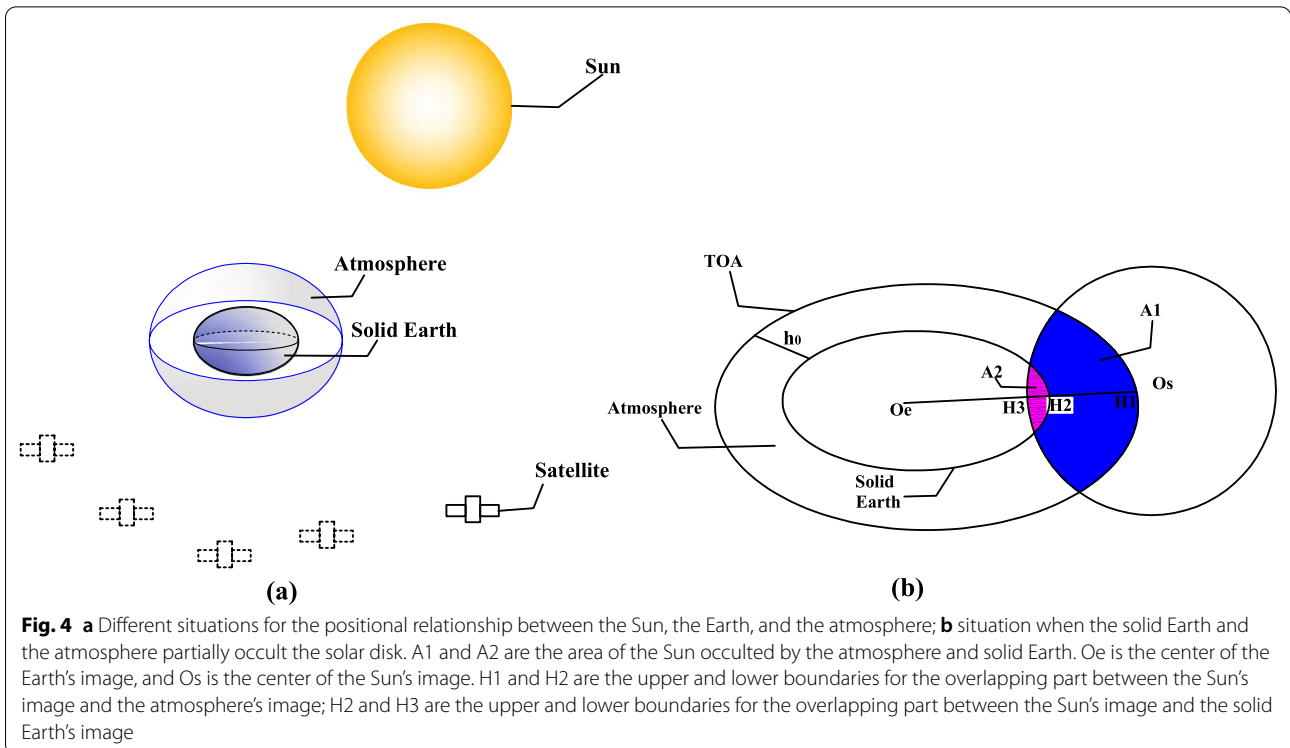$$f(h) = (\mu_2 - \mu_1)\frac{h}{h_0} + \mu_1 \tag{2.2}$$

where h is the distance from any point to the solid Earth in the direction of the center of the solid Earth's projection to the center of the Sun's projection; μ_2, μ_1 represent the radiation reduction coefficients at the boundary of the atmosphere and solid Earth, respectively ($\mu_2 = 1$, $\mu_1 = 0$); h_0 is the height of the Top of Atmosphere (TOA) assumed as an ellipsoid that wraps the solid Earth.

The shadow factor is computed by relative positions between the projections of the Sun, the Earth, and the TOA, which is calculated by applying the perspective projection algorithm to the solid Earth and the TOA ellipsoid separately in Fig. 4. This figure introduces the situation in which the solid Earth and atmosphere partially occult the Sun. Other cases have been described in detail by Li (Li et al. 2019). The shadow factor $\widetilde{\gamma}_0$ in Fig. 4b can be derived as follows:

$$\widetilde{\gamma}_0 = 1 - \frac{0.5(f(H_1) + f(H_2))A_1 + 0.5(f(H_3) + f(H_2))A_2}{\pi \alpha_s^2} \tag{2.3}$$

SOLAARS-CF shadow model

SOLAARS-CF is a curve-fitting shadow model coming from a physical model (SOLAARS) (Robertson et al. 2015). It uses the equatorial radius and polar radius of the Earth to recalculate the spherical radius of the Earth and adjusts the positions of the satellite and the Sun. This method obtains the osculating sphere, which is similar to the Earth's ellipsoid. Thus, the influence of the Earth's oblateness can be included in the eclipse. In addition, the SOLAARS model still considers atmospheric scattering and dissipation effects, including Rayleigh scattering, aerosol dissipation, molecular absorption, and cloud dissipation. However, the input parameters of SOLAARS are enormous, and thus the calculation is complicated. Robertson (2015) used the hyperbolic tangent Sigmoid function proposed by Hubaux et al. (2012) to describe the satellite performance during the eclipse and rebuilt named SOLAARS-CF shadow model by curve fitting of SOLAARS's results. SOLAARS-CF model needs only the

Fig. 4 **a** Different situations for the positional relationship between the Sun, the Earth, and the atmosphere; **b** situation when the solid Earth and the atmosphere partially occult the solar disk. A1 and A2 are the area of the Sun occulted by the atmosphere and solid Earth. Oe is the center of the Earth's image, and Os is the center of the Sun's image. H1 and H2 are the upper and lower boundaries for the overlapping part between the Sun's image and the atmosphere's image; H2 and H3 are the upper and lower boundaries for the overlapping part between the Sun's image and the solid Earth's image

position of the Sun and satellite. The shadow factor can be expressed as below:

$$
\begin{cases}
\widetilde{\gamma}_0 = \dfrac{1+a_1+a_2+a_1 tanh\left(a_3\left(r_E'-a_4\right)\right)+a_2 tanh\left(a_5\left(r_E'-a_6\right)\right)+tanh\left(a_7\left(r_E'-a_8\right)\right)}{2+2a_1+2a_2} \\[4pt]
r_E' = \left\| \left(\overrightarrow{r}_1' - \dfrac{\overrightarrow{r}_2' \bullet \overrightarrow{r}_1'}{\|\overrightarrow{r}_2'\|} * \dfrac{\overrightarrow{r}_2'}{\|\overrightarrow{r}_2'\|} \right) \right\| * \dfrac{p}{R_{osc}} \\[4pt]
d = -\dfrac{\overrightarrow{r}_2' \bullet \overrightarrow{r}_1'}{\|\overrightarrow{r}_2'\|}
\end{cases}
\tag{2.4}
$$

$\widetilde{\gamma}_0$ denote the shadow factor. $(a_1 - a_8)$ are fit coefficients and shown in Table 1; tanh is the hyperbolic tangent function; $\overrightarrow{r}_1'$, $\overrightarrow{r}_2'$ is the adjusted satellite position and the Sun position, respectively; R_{osc} is the adjusted spherical Earth's radius; p is the Earth's equatorial radius; r_E' is the distance from the satellite to the center of the Earth after considering the Earth's oblateness; d is the component of the distance from the satellite to the Earth in the Sun–Earth's direction and is in 10^6m. Table 1 lists an unique set of coefficients which are generated by the trust-region-reflective curve-fitting algorithm (Robertson 2015).

Validation method

SLR is a commonly used mean of external orbital validation (Bury et al. 2019; Hackel et al. 2015). This paper adopts SLR orbit validation and proposes a new mean named ISL orbit check. ISL refers to the interconnection between satellite and satellite through electromagnetic

waves (Maine et al. 2003). After the interconnection, information and data can be shared and transmitted, and the distance between satellites can also be measured. For

BeiDou satellites, the primary purpose of the ISL is to realize the information transmission and two-way range measurement. Once the ground operation control system is not available, the inter-satellite ranging is used to maintain the satellite navigation message updating independently (Maine et al. 2003). Compared with low-speed and wide-beam GPS UHF band ISLs (Rajan 2002; Rajan et al. 2003) and low-speed and wide-beam GLONASS S-band ISLs (Revnivykh, 2012), Ka-band medium-speed ISLs are used in BeiDou constellation (Tang et al. 2018). The BeiDou ISL's ranging accuracy can reach to 0.1–0.3 ns (3–10 cm), and the ISL transmission delay and the receiving delay residual are 0.0084 ns and 0.0399 ns, respectively (Tang et al. 2018; Meng et al. 2017). It is higher than the current BDS orbit accuracy in the along/cross (A/C) direction (10 cm) (Li et al. 2020; http://www.igmas.org/). The observed time is ordinarily different from each other by up to 3 s, and the transformation error from one satellite to another is proved to be less than 4 mm. Therefore, it is necessary to transform the dual one-way measurements at different times into a standard epoch (Tang et al. 2018; Yang et al. 2018). The two-way ISL observation equation is given as follows:

$$
\begin{cases}
p(t_0) = \dfrac{P_{AB}+P_{BA}}{2} = \dfrac{\rho_{AB}(t_0)+\rho_{BA}(t_0)}{2} - c(\Delta_A + \Delta_B) - \dfrac{\delta_{AB}+\delta_{BA}}{2} - \dfrac{\varepsilon_{AB}+\varepsilon_{BA}}{2} \\[4pt]
\Delta_A = \dfrac{D_{RA}+D_{LA}}{2} \\[4pt]
\Delta_B = \dfrac{D_{RB}+D_{LB}}{2}
\end{cases}
\tag{2.5}
$$

P_{AB} and P_{BA} are the distance of satellite A to B and B to A; ρ_{AB} and ρ_{BA} are the pseudo-range values between satellites; t_0 is the common epoch; Δ_A and Δ_B are the hardware delay; c is the velocity of light in vacuum; D_{RB} and D_{LB} are the reception and launch delay of satellite B; D_{RA} and D_{LA} are the reception and launch delay of satellite A; δ_{AB} and δ_{BA} represent observation corrections such as relativistic effect correction and antenna phase center correction; ε_{AB} and ε_{BA} represent observation noise.

The hardware delay is estimated as a constant parameter in the short term (a specific POD arc). However, the parameters may vary when the satellite-related delays are not necessarily equal to each other during different ISL pairs. Therefore, we can directly estimate the ISL-pair-dependent constant parameter Δ_{AB} within a POD arc as follows (Wang et al. 2019):

Table 1 Fit coefficients for the shadow factor

Function	b_1	b_2	b_3	b_4
$a_1 = b_1 e^{b_2 d} + b_3 e^{b_4 d}$	0.1715	− 0.1423	0.01061	− 0.01443
$a_2 = b_1 d + b_2$	0.008162	0.3401	–	–
$a_3 = b_1 e^{b_2 d} + b_3 e^{b_4 d}$	260.9	− 0.4661	27.81	− 0.009437
$a_4 = b_1 d^{b_2} + b_3$	− 0.006119	1.176	6.385	–
$a_5 = b_1 e^{b_2 d} + b_3 e^{b_4 d}$	87.56	− 0.09188	19.30	-0.01089
$a_6 = b_1 d + b_2$	0.002047	6.409	–	–
$a_7 = b_1 e^{b_2 d} + b_3 e^{b_4 d}$	61.98	− 0.1629	27.87	− 0.02217
$a_8 = b_1 e^{b_2 d} + b_3 e^{b_4 d}$	6.413	− 0.0002593	− 0.01479	− 0.1318

Zhang *et al. Earth, Planets and Space*   (2022) 74:126

Page 7 of 14

$$\Delta_{AB} = \frac{D_{RB} + D_{LB} + D_{RA} + D_{LA}}{2} \qquad (2.6)$$

This paper compares the difference between the precision orbit and the ISL results to evaluate the accuracy of the four shadow models. Combining the results of precision orbit determination, the verification equation can be obtained by:

$$\omega(t_0) = \left| \overrightarrow{r}_B(t_0) - \overrightarrow{r}_A(t_0) \right| - P(t_0) \qquad (2.7)$$

$\omega(t_0)$ is the check residual value; $\overrightarrow{r}_B(t_0)$ and $\overrightarrow{r}_A(t_0)$ are satellites' positions in the inertial coordinate system.

Comparison of shadow models and their impact on POD

Data and POD estimation strategy

This paper used the Multi-GNSS EXperiment (MGEX) network data (Montenbruck et al. 2017) in 2019 for the POD of BeiDou satellites. During this period, 50–60 stations received BDS data. The orbit determination adopted non-difference Pseudo-range Combination (PC) and Carrier-phase Combination (LC) observations with a 1-day arc length. All data are processed using the

GNSS analysis software package developed by Shanghai Astronomical Observatory (SHAO). This software uses a least-squares estimator to process GNSS data to generate orbits, clocks, Earth Orientation Parameter (EOP), Solution Independent EXchange Format (SINEX) and other products. It also could implement the SLR orbit validation. The software applies the Box-Wing Solar Radiation Pressure Model (SRPM) and Box-Wing Earth Radiation Pressure Model (ERPM).

The SRPM uses the Box-wing model to calculate the initial value and adds five parameters of the ECOM model
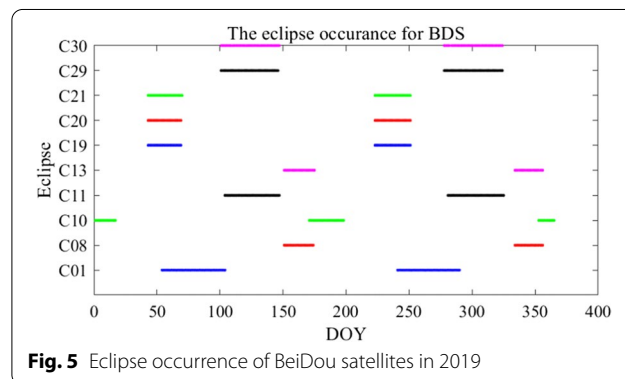
Fig. 5 Eclipse occurrence of BeiDou satellites in 2019

Table 2 Correction models and parameter estimation strategy

	Items	Strategy
Models	Observation	LC + PC(Zero-Differential)
	Interval and arc length	300 s | 1 day
	Cutoff elevation	7°
	Troposphere model	Saastamoinen (DRY) (Liu et al. 2017) | estimated (WET)
	Solid tide; Ocean tide; Pole tide	IERS convention (2010) (Petit and Luzum, 2010)
	Satellite antenna Phase Center Offset (PCO) Receiver antenna PCO | Phase Center Variance (PCV) Mapping function	IGS14.ATX (update to 2020) add with BDS PCO from CSNO/TARC The same with corrections to GPS Global Mapping Function (GMF) (Böhm et al. 2006)
	Site coordinates(priori)	IGS14(psd) (1sigma)
	SRP model Shadow model	SRPM (bw + 5ECOM) (Xi et al. 2018) 3dishes/PPM/PPMatm/SOLAARS-CF
	Ionospheric	1-order removed by LC/PC; higher order corrections of the model (Xi and Wang 2021)
	Earth Radiation Pressure	Considered
	Thermal Radiation Pressure	Considered
	Antenna thrust	Considered
Parameters	Orbit	Estimated
	Satellite clock	Estimated
	Receiver clock	Estimated
	Ambiguity	Zero-differenced ambiguity resolution
	Earth orientation parameter	Estimated x_p, y_p, $\dot{x}_p$, $\dot{y}_p$, Length of Day (LOD)
	Tropospheric parameter	Zenith troposphere delay and gradient parameters are estimated as piecewise constant with 1 h

Zhang *et al. Earth, Planets and Space*   (2022) 74:126

Page 8 of 14

(D0, Y0, B0, BC, and BS) for the BDS satellite (Arnold et al. 2015; Duan and Hugentobler 2021). The ERPM is a numerical model with the measured Earth radiation (albedo and infrared) as the input. The radiation data is calculated according to the formula to obtain the Earth grid's reflection coefficient and thermal infrared radiation coefficient. The radiation data comes from the Clouds and the Earth's Radiant Energy System (CERES) data of NASA. The thermal radiation is considered according to the thermal conditions of each satellite's surface and substituted into the actual thermal environment; the finite element analysis and the average temperature analysis of the surface heat balance method are carried out to calculate the perturbation force of the thermal radiation force. The antenna thrust is also considered. BDS satellite L-band transmit power is taken from the IGS metadata SINEX file (IGSMAIL-8015, from Peter Steigenberger) (Duan et al. 2022).

The other models follow the IERS conventions 2010 or recommended by IGS. The observation types, error correction models, and estimated parameters are listed in Table 2. To facilitate the orbit check, we refer to the satellites with laser observations published by the International Laser Ranging Service (ILRS) and select satellites C01, C08, C10, C11, C13, C19, C20, C21, C29, and C30 to calculate the occurrence of eclipse throughout the year. Figure 5 illustrates the eclipse statistics for these satellites in 2019. The horizontal axis represents the Day of Year (DOY), and the vertical axis represents the eclipse occurrence.

According to the statistics, the Earth's shadowing days for the satellites C01, C08, C10, C11, C13, C20, C21, C29, and C30 were 101 days, 47 days, 58 days, 89 days, 48 days, 56 days, 56 days, 57 days, 93 days and 93 days, respectively. The SRP model was SRPM which was a priori boxwing model. The same attitude equation was used during the eclipse in which C13 and C16 kept yaw-steering (YS), other satellites of BDS-2 IGSO/MEO used yaw-steering orbit-normal (YS-ON), and the switches between YS and ON take place when the sun elevation angle is approximately ± 4 deg (Dai et al. 2015). BDS-3 Shanghai Engineering Center for Microsatellites (SECM) satellites use YS-ON, and BDS-3 China Academy of Space Technology (CAST) satellites keep YS (Li et al. 2020). The yaw control model of CAST satellites was established by Dilssner (2017). The formula for the yaw angle was described as below:

$$\psi_{\mathrm{cast}} = \mathrm{ATAN2}(-\tan\beta_d, \sin\eta) \tag{3.1}$$

where β_d is modified Sun elevation angle:

$$\begin{cases} \beta_d = \beta + f \times (\mathrm{SIGN}(\beta_0, \beta) - \beta) \\ f = \begin{cases} \frac{1}{1+d_m \times \sin^4\eta}, \beta_0 \leq \beta \\ 0, \beta_0 > \beta \end{cases} \end{cases} \tag{3.2}$$

This modified Sun elevation angle ensures a minimum angular distance of β_0 between the Sun's vector and the spacecraft's z-axis. β is the Sun elevation angle, η is the geocentric orbit angle between the satellite and orbit midnight. $\mathrm{SIGN}(\beta_0, \beta)$ is a FORTRAN function returning the value of β_0 with the sign of β. d_m is a dimensionless constant, and equals to 80,000. f is a bell-shaped smoothing function of the orbit angle η.

The SECM attitude control model is given by Xia et al. (2018). When the sun elevation β is within ± 3 deg, the sun vector component S_{oy} can be determined as below:

$$S_{oy} = \begin{cases} -\sin(3\deg), \beta > 0 \\ \sin(3\deg), \beta < 0 \end{cases} \tag{3.3}$$

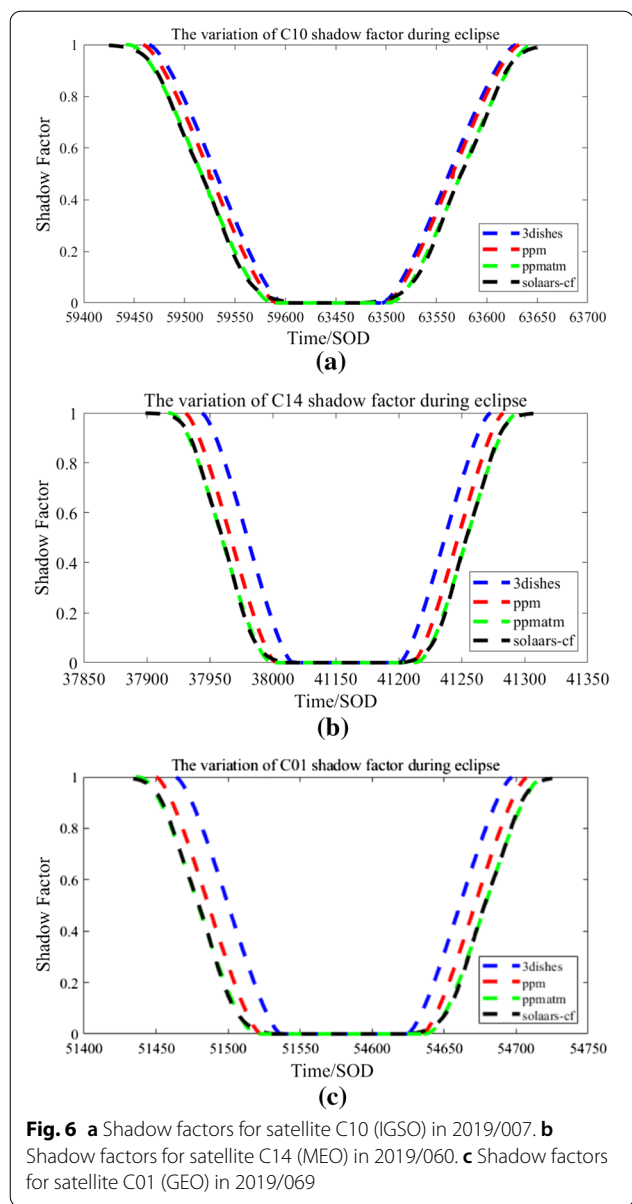The yaw-angle ψ_{secm} is expressed as:

$$\psi_{\mathrm{secm}} = \mathrm{ATAN2}(S_{oy}, \sin\eta\cos\beta) \tag{3.4}$$

Only the shadow model has been changed for comparison without GNSS data, models, and strategy changes. Moreover, the errors in the force model may be absorbed by other estimated parameters. Thus, we avoid using any estimated empirical parameters.

Primarily, multistep integration methods such as the Adams–Cowell (AC) integrator with fixed step size are widely used in GNSS POD (Bhattarai et al. 2019; Huang and Zhou, 1992). However, the traditional AC integrator used in eclipse duration analysis is inaccurate. Although the deficiencies can be partly mitigated by shortening the step size of the traditional AC integrator, the computation cost and round-off errors are still significantly increased with a small step size (Montenbruck et al. 2017). Therefore, the adjustable-step integration method combining multistep and single-step around the eclipse will solve the problems. The output epochs of the modified integrator are kept the same as the traditional AC integrator, but a single-step integrator is activated when the current output epoch is going to enter, pass and leave an eclipse interval (Ju et al. 2017). This paper also adopted this strategy.

Comparison of shadow factor and SRP acceleration

The shadow factor and SRP acceleration derived from four shadow models were compared. Figure 6 shows the shadow factors of different shadow models for the different types of satellites. To make the entire eclipse process
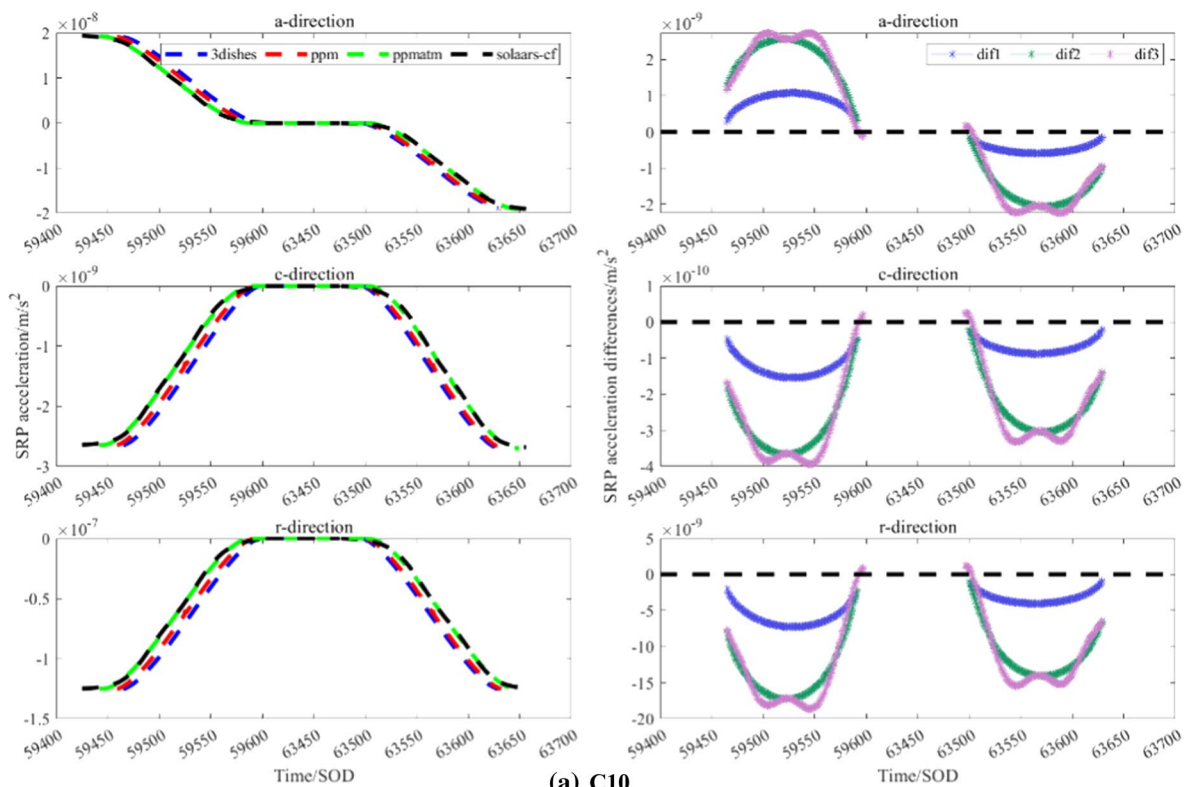
Zhang *et al. Earth, Planets and Space*   (2022) 74:126

Page 9 of 14

Fig. 6 **a** Shadow factors for satellite C10 (IGSO) in 2019/007. **b** Shadow factors for satellite C14 (MEO) in 2019/060. **c** Shadow factors for satellite C01 (GEO) in 2019/069

Table 3 Time the satellite enters and exits the shadow (unit: SOD)

PRN	Model	T_{enter}	T_{umbra}	$T_{penumbra}$	T_{out}
C10 (IGSO)	3dishes	59,465	59,616	63,482	63,629
	PPM	59,459	59,591	63,500	63,632
	PPMatm	59,442	59,591	63,500	63,649
	SOLAARS-CF	59,421	59,604	63,468	63,656
C14 (MEO)	3dishes	37,944	38,015	41,201	41,273
	PPM	37,931	38,002	41,212	41,283
	PPMatm	37,917	38,002	41,212	41,297
	SOLAARS-CF	37,898	38,011	41,195	41,312
C01 (GEO)	3dishes	51,470	51,538	54,625	54,694
	PPM	51,452	51,526	54,632	54,703
	PPMatm	51,430	51,526	54,632	54,721
	SOLAARS-CF	51,423	51,533	54,329	54,729

umbra; $T_{penumbra}$ is the time when the satellite enters penumbra from umbra to full phase; T_{out} is the time when the satellite is back to full phase. Taking C10 as an example, the moments entering shadow estimated from the models 3dishes, PPM, PPMatm, and SOLAARS-CF are 59465 s, 59459 s, 59442 s, and 59421 s, respectively. The latter three models show the satellite enters the shadow 6 s, 23 s, and 56 s earlier than the 3dishes model, respectively. The period of four models in the umbra phase is 3866 s, 3909 s, 3909 s, and 3864 s, respectively. Afterward, the satellite begins to enter the penumbra from the umbra, and the moments of entering the full phase estimated from four models are 63629 s, 63632 s, 63649 s, and 63656 s, respectively. The SOLAARS-CF model enters the eclipse first and leaves the eclipse last. This may be because it is a fitting model and more sensitive to changes of shadow factors.

Figure 7 shows the SRP acceleration variation status. It can be seen PPMatm and SOLAARS-CF models show the highest degree of conformity, and they are distinguishably different from the conical model. The different types of satellites have a similar trend. Figure 7a shows the acceleration changes of the C10 on behalf of IGSO during the eclipse in the direction of a-direction (along trace), c-direction (orbital surface normal), and r-direction (radial trace), and the scale of the *x*-axis has also been adjusted in eclipse. The SRP acceleration gradually decreases during the penumbra phase and becomes nearly zero in the umbra phase. Figure 7b, c shows the acceleration changes of the C14 on behalf of MEO and the C01 on behalf of GEO during the eclipse. The right side of the *y*-axis indicates the SRP acceleration difference: dif1 is the difference between PPM and 3dishes, dif2 is the difference between PPMatm and 3dishes, and dif3 is the difference between SOLAARS-CF and 3dishes.

appear on a figure, the *x*-axis scale of the umbra phase is adjusted, and its unit is Second of Day (SOD). It can be seen from the figure that the satellite's response to radiation from full phase to umbra and from umbra to full phase is a similar and symmetrical changing process. Due to the consideration of the influence of the Earth's oblateness and atmospheric effect, compared with the conical shadow model, the satellites enter the shadow earlier and come out of the shadow later when using the latter three models. Table 3 lists the moment that the satellite enters and exits the different phases. T_{enter} is the moment when the satellite enters the penumbra from full phase to umbra; T_{umbra} is the time when the satellite enters the

(a) C10

(b) C14

Fig. 7 **a** SRP acceleration variation of C10 (IGSO) in eclipse in 2019/007. **b** SRP acceleration variation of C14 (MEO) in eclipse in 2019/060. **c** SRP acceleration variation of C01 (GEO) in eclipse in 2019/069. Each figure is composed of SRP acceleration (left) and their differences (right) between other three models with regard to 3dishes. In each side of figure, including along trace direction (top), cross trace direction (middle) and radial trace direction (bottom)

Zhang *et al. Earth, Planets and Space* (2022) 74:126

Page 11 of 14
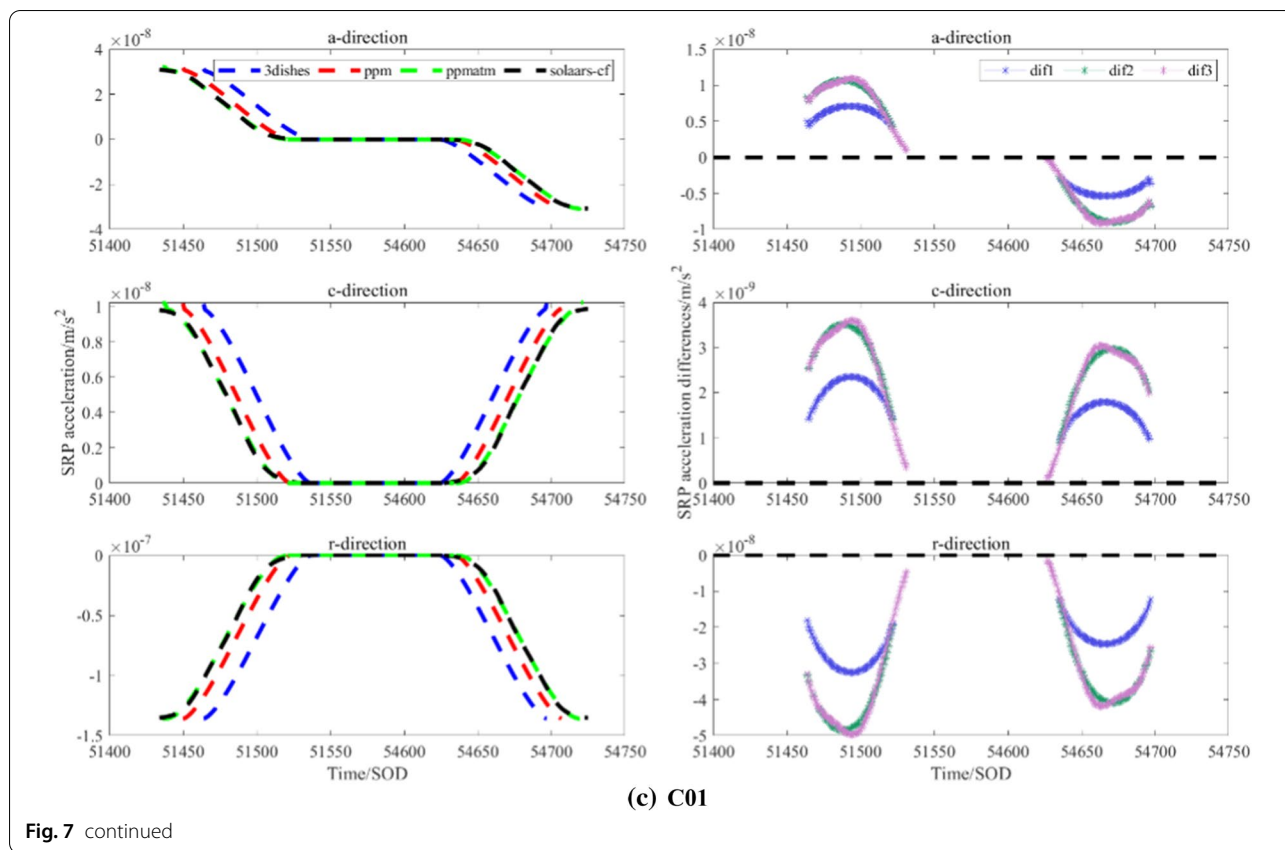
Fig. 7 continued

They show similar characteristics. The acceleration difference between 3dishes and other models is about 10^{-9} m/s^2 in the a-direction and c-direction, and it can reach to 10^{-8} m/s^2 in the r-direction. Therefore, the Earth's oblateness and atmospheric effect must be considered in shadow factor models, especially under present circumstances that perturbation acceleration accuracy stepped toward 10^{-10} m/s^2 (Montenbruck 2020).

SLR orbit validation
To evaluate the impact of the four shadow models on the POD of BeiDou satellites during the eclipse more

Table 4 Satellite center of mass information (unit: mm)

PRN	x-offset	y-offset	z-offset
C08	− 420.3	− 573.5	1100.0
C10	− 426.7	− 573.2	1099.5
C11	− 426.4	− 537.9	1100.0
C13	− 427.1	− 537.9	1100.1
C20	594.7	− 84.6	1264.4
C21	598.6	− 86.6	1265.0
C29	609.5	426.0	614.2
C30	609.7	427.3	615.3

reliably, this paper uses the two-way full rate data of SLR (provided by ILRS) to perform an external check. Before SLR checks (Pearlman et al. 2002), the systematic errors of the original SLR data should be corrected, including the distance errors caused by the tide correction, the atmospheric refraction, the relativistic effect, the distance deviation of the laser reflection points on the surface of the satellite from the Center of Mass (CoM) (which is given in Table 4) and the station systematic deviation. The observation correction follows the models recommended by the IERS convention 2010 (Petit and Luzum 2010), and more information about BDS in International Laser Ranging Service (ILRS) can be obtained at https://ilrs.cddis.eosdis.nasa.gov/missions/satellitemissions/currentmissions/bdm2com.html. Only when the original observation data deducts these errors, the SLR data can be efficiently used for calculating the residual value. The processed SLR data accuracy is around 1 cm (Combrinck 2010), which is higher than the orbit determination accuracy of the BDS in the radial (R) direction (3–5 cm). This paper only compared the SLR validation results in eclipse, because the evaluation of the entire orbital arc will obscure the orbital accuracy of the eclipse period and the duration of the eclipse is small relative to the entire orbital arc. Since there is no corresponding laser

Table 5 SLR validation results of four shadow models for different satellites (N_{points}: Number of observation points; unit: mm)

PRN	Model	Mean	RMS	STD	N_{points}
C08	3dishes	170.5	171.5	18.6	333
	PPM	168.6	169.7	18.6	333
	PPMatm	165.5	166.7	18.6	333
	SOLAARS-CF	165.2	166.5	18.6	333
C10	3dishes	13.1	33.1	30.4	1395
	PPM	7.6	26.1	29.8	1395
	PPMatm	3.6	23.2	29.8	1400
	SOLAARS-CF	3.5	23.2	29.6	1400
C11	3dishes	29.6	61.8	54.3	20,119
	PPM	26.3	59.7	53.6	20,547
	PPMatm	24.7	58.1	53.5	20,595
	SOLAARS-CF	24.3	57.9	53.6	20,612
C13	3dishes	235.5	236.0	15.2	268
	PPM	233.7	233.6	15.1	268
	PPMatm	228.3	228.8	15.1	268
	SOLAARS-CF	226.4	226.9	15.1	268
C20	3dishes	52.5	67.9	52.7	17,202
	PPM	49.7	66.2	52.5	17,229
	PPMatm	47.9	65.5	52.6	17,289
	SOLAARS-CF	47.6	65.3	52.2	17,289
C21	3dishes	22.3	49.9	36.3	2439
	PPM	20.4	48.6	36.1	2439
	PPMatm	19.7	46.5	36.4	2472
	SOLAARS-CF	19.3	46.6	36.5	2472
C29	3dishes	− 23.9	66.3	61.9	16,776
	PPM	− 21.3	64.1	61.8	16,776
	PPMatm	− 19.5	62.5	61.6	16,776
	SOLAARS-CF	− 19.9	62.7	61.6	16,776
C30	3dishes	− 44.0	48.3	20.2	15,580
	PPM	− 41.5	46.5	20.2	15,580
	PPMatm	− 40.8	45.8	20.2	15,580
	SOLAARS-CF	− 40.2	45.5	20.3	15,580

Table 6 Transmitting and receiving information of ISL

Time period (DOY)	Transmitting	Eclipse (Yes or No)	Receiving	Eclipse (Yes or No)
043–070	C19	Yes	C23	No
043–070	C21	Yes	C23	No
102–118	C27	Yes	C22	No
102–118	C30	Yes	C23	No

observation data for C01 and C19 during the eclipse, this paper has calculated the SLR check results of the remaining 8 satellites. All the results of selected satellites are

Table 7 Performance of different shadow models by ISL check (N_{points}: Number of observation points; unit: mm)

ISL	Shadow model	Mean	RMS	STD	N_{points}
C19–C23	3dishes	− 68.2	110.4	86.8	1583
	PPM	− 64.0	108.6	87.0	1586
	PPMatm	− 62.0	107.6	87.2	1591
	SOLAARS-CF	− 62.3	107.8	87.1	1591
C21–C23	3dishes	− 75.1	115.5	87.9	1068
	PPM	− 73.5	112.6	87.6	1077
	PPMatm	− 71.4	111.1	88.0	1083
	SOLAARS-CF	− 71.6	111.2	88.0	1083
C27–C22	3dishes	− 46.4	106.3	95.7	597
	PPM	− 42.1	102.2	94.9	597
	PPMatm	− 38.6	100.1	94.6	601
	SOLAARS-CF	− 38.3	99.5	94.5	601
C30–C22	3dishes	− 5.5	121.3	118.2	961
	PPM	− 4.1	118.7	117.9	961
	PPMatm	− 3.3	116.5	117.6	961
	SOLAARS-CF	− 3.1	116.4	117.5	961

depicted in Table 5. It can be seen the PPM, PPMatm and SOLAARS-CF have smaller residual values than that of 3dishes. The mean value can be decreased by up to 10 mm (C10), and the rest are generally decreased by 2–6 mm; the RMS value can be decreased by up to 10 mm (C10), and the rest are generally 2–5 mm. Comparing the SLR check results of the PPMatm and SOLAARS-CF models, the accuracy of the two models is comparable and better than that of the other two models. The performance of the validation result of C08 and C13 is not well, and this may be due to inadequate data and the low data quality. The SLR calculation results of all satellites are showed in Additional file 1.

ISL check

The ISL measurements of BeiDou Satellites from DOY 032 to DOY 120 in 2019 are chosen to check the precision of the BeiDou satellite orbit during the eclipse in this period. C19, C21, C27, and C30 are selected as the objectives in this paper. Table 6 gives the satellite information of ISL. To better evaluate the shadow models, we keep only transmitting satellites are eclipsing. Table 7 lists the ISL check results. The orbit accuracy of PPM, PPMatm, and SOLAARS-CF is higher than 3dishes, and PPMatm and SOLAARS-CF are better than other two models. The mean value is decreased by up to 8 mm for C27, and generally decreased by 2–6 mm for the others. The RMS value is decreased by up to 7 mm for C27, and generally decreased by 2–5 mm. The ISL calculation results of all links are showed in Additional file 1.

Conclusions

This paper first introduces shadow models' modelling methods, including conical, PPM, PPMatm, and SOLAARS-CF models. PPM is modelled with consideration of the Earth's oblateness based on the perspective projection algorithm; PPMatm considers the atmospheric effect by linear equations for solar radiation reduction based on PPM; SOLAARS-CF takes the Earth's oblateness and atmospheric effect into consideration by a curve fitting from a physical-based model (SOLAARS). And then, the shadow factor and SRP acceleration derived by the four shadow models are compared. The satellite enters shadow earlier and comes out of shadow later by PPM, PPMatm, and SOLAARS-CF models than by 3dishes. The SRP acceleration derived from PPMatm and SOLAARS-CF models distinguish with that of 3dishes, and the PPMatm and SOLAARS-CF models have the highest conformity. To further verify the four shadow models, this paper used two validation methods: SLR check and ISL check. It is noteworthy that the ISL check is a new method proposed by this paper. As the result of the SLR check, the shadow models with the Earth's oblateness and atmospheric effects (PPMatm, SOLAARS-CF) have an improvement of 2–10 mm in RMS compared with the conical model. The ISL check results show that PPMatm and SOLAARS-CF are better than the other two models. Compared with the 3dishes model, the RMS value can be generally decreased by 2–7 mm. The performance of the PPMatm and SOLAARS-CF models is comparable. From the perspective of computational cost, the four models do not have many differences, and the input parameters are the position of the satellite, the Sun, and the Lunar. With the consideration of the precision and reliability of the modelling in eclipse, PPMatm and SOLAARS-CF are recommended for POD processing, and the Earth's oblateness and atmospheric effect must be taken into consideration in shadow models, especially in the current situation of perturbation acceleration accuracy stepping toward 10^{-10} m/s^2.

Supplementary Information

The online version contains supplementary material available at https://doi.org/10.1186/s40623-022-01684-5.

Additional file 1. Figure S1. (a) SLR check results of all satellites. The y-axis (left) is the omc value; the y-axis (right) is the sun elevation angle; the x-axis is the DOY. **Figure S2.** (b) ISL results of all links. The y-axis is the check omc value; the x-axis is the DOY.

Declarations

Competing interests
The authors declare that they have no conflict of interest.

Author details
[1] Astro-Geodynamics Research Center, Shanghai Astronomical Observatory, Chinese Academy of Sciences, Shanghai 200030, China. [2] University of Chinese Academy of Sciences, Beijing 100049, China. [3] Shanghai Key Laboratory of Space Navigation and Positioning Techniques, Shanghai 200030, China. [4] Department of Geomatics Engineering, University of Calgary, 2500 University Drive, N.W., Calgary, AB T2N1N4, Canada. [5] Key Laboratory of Satellite Navigation and Mobile Communication, Research Institute for Frontier Science, Beihang University, Beijing 100191, China.

References
Adhya S, Sibthorpe A, Ziebart M et al (2004) Oblate earth eclipse state algorithm for low-earth-orbiting satellites. J Spacecr Rocket 41(1):157–159. https://doi.org/10.2514/1.1485

Arnold D, Meindl M, Beutler G, Dach R, Schaer S, Lutz S, Prange L, Sośnica K, Mervart L, Jäggi A (2015) CODE's new solar radiation pressure model for GNSS orbit determination. J Geodesy 89(8):775–791. https://doi.org/10.1007/s00190-015-0814-4

Bhattarai S, Ziebart M, Allgeier S, Grey S, Springer T, Harrison D, Li Z (2019) Demonstrating developments in high-fidelity analytical radiation force modelling methods for spacecraft with a new model for GPS IIR/IIR-M. J Geodesy 93(9):1515–1528. https://doi.org/10.1007/s00190-019-01265-7

Böhm J, Niell A, Tregoning P, Schuh H (2006) Global Mapping Function (GMF): a new empirical mapping function based on numerical weather model data. Geophys Res Lett. https://doi.org/10.1029/2005GL025546

Bury G, Sośnica K, Zajdel R (2019) Multi-GNSS orbit determination using satellite laser ranging. J Geodesy 93(12):2447–2463. https://doi.org/10.1007/s00190-018-1143-1

Combrinck L (2010) Satellite laser ranging. In: Guochang X (ed) Sciences of geodesy-I. Springer, Berlin, pp 301–338. https://doi.org/10.1007/978-3-642-11741-1_9

Dai X, Ge M, Lou Y, Shi C, Wickert J, Schuh H (2015) Estimating the yaw-attitude of BDS IGSO and MEO satellites. J Geod 89(10):1005–1018. https://doi.org/10.1007/s00190-015-0829-x

Dilssner F (2017) A note on the yaw attitude modeling of BeiDou IGSO-6, a report dated November 20, 2017. http://navigation-ofce.esa.int/attachments_24576369_1_BeiDou_IGSO-6_Yaw_Modeling.pdf

Zhang *et al. Earth, Planets and Space* (2022) 74:126

Page 14 of 14

Duan B, Hugentobler U (2021) Enhanced solar radiation pressure model for GPS satellites considering various physical effects. GPS Solut 25(2):1–14. https://doi.org/10.1007/s10291-020-01073-z

Duan B, Hugentobler U, Selmke I, Marz S, Killian M, Rott M (2022) BeiDou satellite radiation force models for precise orbit determination and geodetic applications. IEEE Trans Aerosp Electron Syst. https://doi.org/10.1109/TAES.2021.3140018

Ferraz-Mello S (1972) Analytical study of the Earth's shadowing effects on satellite orbits. Celest Mech 5(1):80–101. https://doi.org/10.1007/BF01227825

Hackel S, Steigenberger P, Hugentobler U, Uhlemann M, Montenbruck O (2015) Galileo orbit determination using combined GNSS and SLR observations. GPS Solut 19(1):15–25. https://doi.org/10.1007/s10291-013-0361-5

Huang TY, Zhou QL (1992) Adams-Cowell integrator with a first sum. Chin Astron Astrophys 17(2):205–213. https://doi.org/10.1016/0275-1062(93)90071-V

Hubaux C, Lemaitre A, Delsate N, Carletti T (2012) Symplectic integration of space debris motion considering several earths shadowing models. Adv Space Res 49(10):1472–1486. https://doi.org/10.1016/j.asr.2012.02.009

Ju B, Gu D, Herring TA, Allende-Alba G, Montenbruck O, Wang Z (2017) Precise orbit and baseline determination for maneuvering low earth orbiters. GPS Solut 21(1):53–64. https://doi.org/10.1007/s10291-015-0505-x

Kozai Y (1963) Effects of solar radiation pressure on the motion of an artificial satellite. Smithsonian Contributions to Astrophysics, 6, 109. https://ntrs.nasa.gov/citations/19980227979

Li Z, Ziebart M, Bhattarai S, Harrison D (2019) A shadow function model based on perspective projection and atmospheric effect for satellites in eclipse. Adv Space Res 63(3):1347–1359. https://doi.org/10.1016/j.asr.2018.10.027

Li X, Yuan Y, Zhu Y, Jiao W, Bian L, Li X, Zhang K (2020) Improving BDS-3 precise orbit determination for medium earth orbit satellites. GPS Solutions 24(2):1–13. https://doi.org/10.1007/s10291-020-0967-3

Liu J, Chen X, Sun J, Liu Q (2017) An analysis of GPT2/GPT2w+ Saastamoinen models for estimating zenith tropospheric delay over Asian area. Adv Space Res 59(3):824–832. https://doi.org/10.1016/j.asr.2016.09.019

Maine KP, Anderson P, Langer J (2003) Crosslinks for the next-generation GPS. IEEE Aerospace Conference 4:1589–1596. https://doi.org/10.1109/AERO.2003.1235087

Meng Z, Yang J, Guo X, Hu M (2017) Phase compensation sensor for ranging consistency in inter-satellite links of navigation constellation. Sensors 17(3):461. https://doi.org/10.3390/s17030461

Montenbruck O (2020) IGS white paper on satellite and operations information for generation of precise GNSS orbit and clock products. https://kb.igs.org/hc/en-us/articles/360039337432-IGS-White-Paper-on-Satellite-and-Operations-Information-for-Generation-of-Precise-GNSS-Orbit-and-Clock-Products-2020

Montenbruck O, Gill E, Lutze F (2002) Satellite orbits: models, methods, and applications. ASME Appl Mech Rev 55(2):B27–B28. https://doi.org/10.1115/1.1451162

Montenbruck O, Steigenberger P, Prange L, Deng Z, Zhao Q, Perosanz F, Romero I, Noll C, Stürze A, Weber G, Schmid R, MacLeod K, Schaer S (2017) The Multi-GNSS Experiment (MGEX) of the International GNSS Service (IGS)–achievements, prospects and challenges. Adv Space Res 59(7):1671–1697. https://doi.org/10.1016/j.asr.2017.01.011

Musen P (1960) The influence of the solar radiation pressure on the motion of an artificial satellite. J Geophys Res 65(5):1391–1396. https://doi.org/10.1029/JZ065i005p01391

Oswald H, Kropatsch W, Leberl F (1982) A perspective projection algorithm with fast evaluation of visibility for discrete three-dimensional scenes. In: Prewitt JMS (Eds.), 1st International Symposium on Medical Imaging and Image Interpretation, Berlin, Germany, pp.464–470. https://doi.org/10.1117/12.934687

Pearlman MR, Degnan JJ, Bosworth JM (2002) The international laser ranging service. Adv Space Res 30(2):135–143. https://doi.org/10.1016/S0273-1177(02)00277-6

Petit G, Luzum B (2010) IERS conventions (2010). Bureau International des Poids et mesures sevres (France). https://www.iers.org/IERS/EN/Publications/TechnicalNotes/tn36.html-1.htm?nn=94912

Rajan JA (2002) Highlights of GPS II-R autonomous navigation. In Proceedings of the 58th Annual Meeting of The Institute of Navigation and CIGTF 21st Guidance Test Symposium (2002). pp. 354–363. https://www.ion.org/publications/abstract.cfm?articleID=969

Rajan J, Orr M, Wang P (2003) On-Orbit Validation of GPS IIR Autonomous Navigation. Proceedings of the Institute of Navigation 59th Annual Meeting, 23–25 June 2003, pp. 411-419. https://www.ion.org/publications/abstract.cfm?articleID=3874

Revnivykh S (2012) GLONASS status and modernization. In Proceedings of ION GNSS 2012, Nashville, TN, pp 3931–3949. https://www.unoosa.org/pdf/icg/2012/icg-7/3-1.pdf

Robertson RV (2015) Highly Physical Solar Radiation Pressure Modeling During Penumbra Transitions (Ph. D thesis). Faculty of the Virginia Polytechnic Institute and State University. https://vtechworks.lib.vt.edu/bitstream/handle/10919/73537/Robertson_RV_D_2015.pdf

Robertson RV, Shoemaker MA (2014) Highly Physical Penumbra Solar Radiation Pressure Modeling and the Earth Flyby Anomaly. 13th International Conference on Space Operations 2014. https://doi.org/10.2514/6.2014-1881

Robertson R, Flury J, Bandikova T, Schilling M (2015) Highly physical penumbra solar radiation pressure modeling with atmospheric effects. Celest Mech Dyn Astron 123(2):169–202. https://doi.org/10.1007/s10569-015-9637-0

Rodriguez-Solano CJ, Hugentobler U, Steigenberger P (2012) Adjustable box-wing model for solar radiation pressure impacting GPS satellites. Adv Space Res 49(7):1113–1128. https://doi.org/10.1016/j.asr.2012.01.016

Tang C, Hu X, Zhou S, Liu L, Pan J, Chen L, Guo R, Zhu L, Hu G, Li X, He F, Chang Z (2018) Initial results of centralized autonomous orbit determination of the new-generation BDS satellites with inter-satellite link measurements. J Geodesy 92(10):1155–1169. https://doi.org/10.1007/s00190-018-1113-7

Villiger A, Dach R (2021) International GNSS Service Technical Report 2020 (IGS Annual Report). IGS Central Bureau and University of Bern; Bern Open Publishing. https://doi.org/10.48350/156425. https://igs.org/news/igs-technical-report-2020/

Vokrouhlicky D, Farinella D, Mignard F (1993) Solar radiation pressure perturbations for Earth satellites, I. A complete theory including penumbra transitions. Astron Astrophys 280:295–312

Vokrouhlicky D, Farinella D, Mignard F (1994) Solar radiation pressure perturbations for Earth satellites, II. An approximate method to model penumbra transitions and their long-term orbital effects on LAGEOS. Astron Astrophys 285:333–343

Vokrouhlicky D, Farinella D, Mignard F (1996) Solar radiation pressure perturbations for Earth satellites, IV. Effects of the Earth's polar flattening on the shadow structure and the penumbra transitions. Astron Astrophys 307:635–644

Wang C, Zhao Q, Guo J, Liu J, Chen G (2019) The contribution of inter-satellite links to BDS-3 orbit determination: model refinement and comparisons. Navigation 66(1):71–82. https://doi.org/10.1002/navi.295

Xi K, Wang X (2021) Higher order ionospheric error correction in BDS precise orbit determination. Adv Space Res 67(12):4054–4065. https://doi.org/10.1016/j.asr.2021.02.002

Xi K, Wang X, Zhao Q (2018) Study on solar radiation pressure model considering the yaw attitude of the BDS. *China satellite navigation conference (csnc) 2018 proceedings* (pp. 265–274). Singapore: Springer Singapore. https://doi.org/10.1007/978-981-13-0014-1_23

Xia L, Lin B, Liu Y, Xiong S, Bai T (2018) Satellite geometry and attitude mode of MEO satellites of BDS-3 developed by SECM. In: Proceedings of the ION GNSS 2018, Institute of Navigation, Miami, pp 1268–1289. https://doi.org/10.33012/2018.16118

Yang Y, Yang X, Li J, Yang C (2018) Progress and performance evaluation of BeiDou Global Navigation Satellite System: data analysis based on BDS-3 demonstration system. Sci China Earth Sci 61(5):614–624. https://doi.org/10.1007/s11430-017-9186-9

Zhang Y, Wang X, Xi K, Shao F (2019) Impact analysis of solar irradiance change on precision orbit determination of navigation satellites. Trans Nanjing Univ Aeronaut Astronaut 36(6):13. https://doi.org/10.16356/j.1005-1120.2019.06.002

Publisher's Note